

Energy, centrality and momentum dependence of dielectron production at collider energies in a coarse-grained transport approach

Stephan Endres,* Hendrik van Hees, and Marcus Bleicher

Frankfurt Institute for Advanced Studies, Ruth-Moufang-Straße 1, D-60438 Frankfurt, Germany and

Institut für Theoretische Physik, Universität Frankfurt,

Max-von-Laue-Straße 1, D-60438 Frankfurt, Germany

(Dated: May 18, 2022)

Dilepton production in heavy-ion collisions at collider energies—i.e., for the Relativistic Heavy-Ion Collider (RHIC) and the Large Hadron Collider (LHC)—is studied within an approach that uses coarse-grained transport simulations to calculate thermal dilepton emission applying in-medium spectral functions from hadronic many-body theory and partonic production rates based on lattice calculations. The microscopic output from the Ultra-relativistic Quantum Molecular Dynamics (UrQMD) model is hereby put on a grid of space-time cells which allows to extract the local temperature and chemical potential in each cell via an equation of state. The resulting dilepton spectra are in good agreement with the experimental results for the range of RHIC energies, $\sqrt{s_{NN}} = 19.6 - 200$ GeV. The comparison of data and model outcome shows that the newest measurements by the PHENIX and STAR Collaborations are consistent and that the low-mass spectra can be described by a cocktail of hadronic decay contributions together with thermal emission from broadened vector-meson spectral functions and from the Quark-Gluon Plasma phase. Predictions for dilepton results at LHC energies show no significant change of the spectra as compared to RHIC, but a higher fraction of thermal contribution and harder slopes of the transverse momentum distributions due to the higher temperatures and flow obtained.

PACS numbers: 25.75.Cj, 24.10.Lx

Keywords: Dilepton production, Monte Carlo simulations

I. INTRODUCTION

A better understanding of the phase structure of strongly interacting matter given by the fundamental theory of Quantum Chromodynamics (QCD) is one of the main goals of heavy-ion experiments at ultra-relativistic energies [1–5]. The collision of two nuclei produces a fireball of hot and dense matter, which typically lives for a time span of several fm/c until the system has cooled, due to collective expansion, to a point where the single particles do not further interact (freeze-out) [6]. The trajectory of the system within the QCD phase diagram is determined by the collision energy: While for lab-frame energies of few GeV one obtains rather low temperatures but finds high values of baryochemical potential, the situation becomes different when going to much higher collision energies; here the temperature increases while the baryochemical potential decreases.

As hadronic observables usually only reflect the properties of the system at the moment of freeze-out, electromagnetic probes are the appropriate tool to obtain information from the earlier stages of the reaction, when the system is at high temperatures and/or net-baryon densities [7, 8]. Since photons and dileptons do not interact strongly, they leave the fireball undisturbed once they are produced. However, in consequence the measurement of electromagnetic probes only gives a time integral over the various stages and sources during the evolution of

the reaction. From the theoretical viewpoint the understanding of the production of electromagnetic probes in a heavy-ion collision is complicated by the fact that the evolving fireball of hot and dense matter is not a static but a highly dynamical non-equilibrium system. However, no fully self-consistent approach to describe the in-medium dilepton production for the out-of-equilibrium case is available today. Consequently one has to apply model descriptions, which always means a reduction of the complexity of the problem to a level where it can be solved.

While hydrodynamic [9, 10] and fireball models [11, 12] in general are successful in describing the measured dilepton spectra by the STAR [13–15] and PHENIX [16] collaborations at RHIC, these models completely rely on a macroscopic description of the fireball. The application of thermal emission rates is usually straightforward in these models, but they require external assumptions such as an initial state and an additional description for the final-state interactions. Besides, their application at lower temperatures and densities is questionable. On the other hand, a full microscopic description of the electromagnetic emission—as it is realized in transport models [17–21] based on kinetic theory—is theoretically challenging, especially at very high collision energies. On the one hand, a fully coherent implementation of the different interfering processes and a correct off-shell treatment of the particles has not yet been obtained; on the other hand, it is also still unknown how the microscopic transition from the hadronic to the partonic phase (and vice versa) is actually realized in QCD. Nevertheless there exist several approaches which aim for such an advanced microscopic

* endres@th.physik.uni-frankfurt.de

description including off-shell and medium effects [22–28].

The coarse-graining approach, which is used in the present work for the theoretical calculation of dilepton production, is based on the concepts presented in Ref. [29] and has been successfully applied to describe spectra of electromagnetic probes at SIS 18, FAIR and SPS energies [30–33]. It offers a compromise between the microscopic and macroscopic description of the collision evolution. On the one hand the dynamics is here based on a purely microscopic description from the Ultrarelativistic Quantum Molecular dynamics (UrQMD) model [34, 35], on the other hand the “coarse-graining” (i.e., the reduction of the large amount of information regarding the phase-space coordinates of the single hadrons)—performed by averaging over a large ensemble events and extracting the local thermodynamic properties of the system—allows to describe the reaction dynamics in macroscopic terms of temperature and chemical potential. However, it has the advantage that it is in principle applicable to all phases of a heavy-ion collision and also works for lower collision energies where the use of other macroscopic models is questionable.

For the present paper previous studies are extended to energies available at the Relativistic Heavy-Ion Collider (RHIC) and the Large Hadron Collider (LHC), which covers the range of center-of-momentum energies from $\sqrt{s_{NN}} = 19.6 \text{ GeV}$ up to 5500 GeV . In this energy regime the net-baryon density is assumed to be close to zero for the greatest part of the fireball evolution, and a significant amount of the electromagnetic emission will stem from the Quark-Gluon Plasma (QGP). The specific conditions found at these collision energies offer the possibility to study—among others—the following issues:

- The experimental dilepton measurements will show whether the hadronic spectral functions, which have proven to successfully describe the low-mass dilepton excess, are also consistent with the conditions found in heavy-ion collisions at collider energies, where the baryochemical potential is significantly lower than the temperature for the greatest part of the reaction evolution. Previous work has shown that the in-medium effects on the spectral properties of baryon resonances should still play an important role since the modification of vector mesons is governed by the *sum* of the baryon and anti-baryon densities, not the net density [11].
- At higher invariant masses ($M_{e^+e^-} > 1 \text{ GeV}/c^2$) correlated open-charm decays give a significant contribution to the measured dilepton yield for RHIC and LHC energies [36]. Similar to the light vector mesons, whose spectral shape is modified in the medium, the charm contribution is known to be affected by the presence of a hot and dense medium [37–39]. However, it is unclear how strong these effects are. A direct measurement is difficult, as one also finds a strong thermal contribution from the

QGP in that mass region. It is therefore an important theoretical task to disentangle the different contributions and to provide a comprehensive description of the measured dilepton spectra. Although we do not consider charm contributions in the present study, the thermal results for the QGP contribution may serve as a baseline and help to limit the possible medium modifications for D and \bar{D} mesons.

- Due to the very high temperatures reached at the collider energies considered here, the partonic contribution to the overall dilepton yield will be much more dominant than at lower energies. This might facilitate to study the properties of the Quark-Gluon Plasma, e.g., its temperature [11, 40].
- Further, it will be interesting whether the reaction dynamics of the colliding system shows deviations as compared to the situation at lower energies. Large parts of the evolution are dominated by the Quark-Gluon Plasma, in contrast to the situation at SPS or even SIS 18 and FAIR. Experimental results for RHIC exhibited an unexpected large flow for direct photons, which is not fully explained by theory up to now [41, 42]. With regard to the coarse-graining approach it will be especially interesting to see in how far the underlying microscopic dynamics, which is completely hadronic, can account for the correct expansion of the system and the time-evolution of temperature and chemical potential.

This paper is structured as follows. In Sec. II the coarse-graining approach is introduced, and the various dilepton-production mechanisms, which enter the calculations, are outlined. This is followed by a presentation of the results for the space-time evolution of the reaction (Sec. III A) and dilepton spectra for RHIC and LHC energies (in III B and III C). A comparison of the results for RHIC and LHC is given in Sec. III D. Finally, we conclude with a summary and an outlook to further studies in section IV.

II. THE COARSE-GRAINING APPROACH

In the following, the basic features of the coarse-graining approach are outlined. This description is kept concise here, as the same model was in detail presented previously; for details we refer the reader to Refs. [30–32].

A. Thermal properties from microscopic simulations

As a first step, simulations for the different collision energies are conducted with the present version

3.4 of the Ultra-relativistic Quantum Molecular Dynamics (UrQMD) approach [34, 35, 43, 44], a semi-classical hadronic transport model based on the concepts of kinetic theory, in which the evolution of a heavy-ion collision is described by the propagation of on-shell particles on relativistic trajectories in combination with a stochastic treatment of the individual particle scattering processes. The model offers an effective solution for the relativistic Boltzmann equation, where the collision term includes elastic and inelastic scatterings as well as resonance decays. To account for quantum statistics, the hadrons are represented by Gaussian wave packets and effects such as, e.g., Pauli blocking are included. The model includes 32 meson and 55 baryon resonance species with a mass up to $2.3 \text{ GeV}/c^2$; the corresponding resonance parameters and cross-sections are adapted and extrapolated to the values collected by the Particle Data Group [45]. To include excitations with higher masses, a continuous spectrum of pseudo-resonances from meson-baryon interactions with energies up to $\sqrt{s} = 3 \text{ GeV}$ is implemented, while hadron-hadron collisions with higher energies are treated via string excitation.

Note that within the UrQMD model one has a well determined phase-space distribution function $f(\vec{x}, \vec{p}, t)$, as the positions and momenta of all particles are known. However, since the full microscopic treatment of the medium effects is quite complicated, the present approach aims to reduce (i.e., to coarse-grain) the amount of information given by $f(\vec{x}, \vec{p}, t)$, such that one can switch from a microscopic to a macroscopic description of the collision. Instead of the individual particle phase-space coordinates, the system is then defined by its thermodynamic properties. To do so, it is first necessary to obtain a smooth distribution function, which is realized by averaging over a large number of events:

$$f(\vec{x}, \vec{p}, t) = \left\langle \sum_h \delta^{(3)}(\vec{x} - \vec{x}_h(t)) \delta^{(3)}(\vec{p} - \vec{p}_h(t)) \right\rangle. \quad (1)$$

Here the angle brackets $\langle \rangle$ denote the ensemble average. It is important to bear in mind that the UrQMD model constitutes a non-equilibrium approach, whereas the thermodynamic properties are well defined only for equilibrated matter. Consequently, the approximate extraction of equilibrium quantities is consistent only locally. Thus a grid of small space-time cells is set-up where—following Eq. 1—for each of these cells the baryon current and energy-momentum tensor are extracted as

$$\begin{aligned} T^{\mu\nu} &= \frac{1}{\Delta V} \left\langle \sum_{i=1}^{N_h \in \Delta V} \frac{p_i^\mu \cdot p_i^\nu}{p_i^0} \right\rangle, \\ j_B^\mu &= \frac{1}{\Delta V} \left\langle \sum_{i=1}^{N_B \in \Delta V} \pm \frac{p_i^\mu}{p_i^0} \right\rangle. \end{aligned} \quad (2)$$

Here ΔV is the volume of the cell, and the sum is taken over all hadrons or (anti-)baryons in the cell, respectively.

If one knows j_B^μ and $T^{\mu\nu}$, the local rest frame (LRF) can be determined by applying the definition of Eckart [46], which requires a vanishing baryon flow $\vec{j}_B = 0$. The energy and net-baryon density of the cell are then defined as $\varepsilon = T_{\text{LRF}}^{00}$ and the baryon density is $\rho_B = j_{B,\text{LRF}}^0$.

To obtain temperature and baryochemical potential it is necessary to apply an equation of state (EoS) which translates the local energy and baryon densities into T and μ_B . For consistency with the underlying transport model, we apply a hadron gas EoS [47] for the lower temperature range up to $T = 170 \text{ MeV}$. It includes the same hadronic degrees of freedom as the UrQMD approach. For higher temperatures a pure hadronic description is insufficient, as the phase transition to a Quark-Gluon Plasma also changes the degrees of freedom and consequently the equation of state. We therefore use an EoS from Lattice calculations [48] (with a critical temperature $T_c = 170 \text{ MeV}$) for cells with higher energy densities. While both EoS match in the temperature region from 150-170 MeV, the Lattice EoS gives significantly higher temperatures for very hot cells.

B. Non-equilibrium effects

The approach as outlined above assumes a locally equilibrated system in each cell. However, it is clear that within a transport approach this condition is not always fulfilled in a satisfying manner. In contrast, due to the non-equilibrium nature of the model one finds significant deviations from kinetic and/or chemical equilibrium. For a correct description of the fireball evolution the consequences of these deviations need to be considered. Basically one finds two relevant effects which affect the thermodynamic properties and, consequently, the dilepton emission:

1. Pressure isotropy is necessary for a system to be in *kinetic equilibrium*. However, it is well known from previous studies [49, 50] that the initial stages of a heavy-ion collision are dominated by large differences between the longitudinal and transverse pressures. This is a consequence of the strong longitudinal compression of the nuclei at the beginning of the collision. In this case, the energy density is overestimated in the cell, as a large fraction of the energy is of no relevance with regard to the thermal properties of the system. To apply the coarse-graining approach also for the first few fm/c of the collision, it is therefore necessary to extract a realistic energy density ε_{eff} taking the limited degree of thermalization into account. This is achieved by the use of a generalized equation of state for a Boltzmann-like system [51, 52], that gives ε_{eff} in dependence on the “bare” energy density in the cell and the pressure anisotropy. The results for SPS energies showed that significant deviations of ε_{eff} are only found for the first 1-2 fm/c of the collision [30].

2. *Chemical non-equilibrium* shows up in the form of finite meson chemical potentials (in full equilibrium, all meson chemical potentials vanish as the meson number is not a conserved quantity, in contrast to, e.g., the net-baryon number) and most dominantly in form of a pion chemical potential μ_π , since the π mesons are the most abundantly produced particles. A finite μ_π is the consequence of an overpopulation of pion states. In a transport model, such an over-dense pion system is especially found at the very beginning of the reaction, when the fireball is still far from kinetic equilibrium and the first inelastic collisions produce a large number of pions [53]. The pion chemical potential is important for the population of ρ and ω vector mesons, as a high density of pions increases the probability for the production of these particles (besides, μ_π has also some moderate effects on the spectral shape) [54, 55]. To account for these effects we extract the pion chemical potential in each cell in Boltzmann approximation.

C. Thermal dilepton rates

The thermal emission of dileptons from an equilibrated system of hot and dense matter is determined by the imaginary part of the (retarded) electromagnetic current-current correlation function, $\text{Im } \Pi_{\text{em}}^{(\text{ret})}$, which is related to the electromagnetic current j_μ [56]. The dilepton yield per four-volume and four-momentum can then be calculated according to the relation [55, 57]

$$\frac{dN_{ll}}{d^4x d^4q} = -\frac{\alpha_{\text{em}}^2 L(M)}{\pi^3 M^2} f_B(q; T) \text{Im } \Pi_{\text{em}}^{(\text{ret})}(M, \vec{q}; \mu_B, T), \quad (3)$$

where f_B is the Bose distribution function and $L(M)$ the lepton phase space.

In the hadronic low-mass regime (i.e., for $M < 1 \text{ GeV}/c^2$) the electromagnetic current directly couples to the vector mesons and—assuming vector meson dominance (VMD)— Π_{em} is proportional to the vector-meson propagator

$$D_V = \frac{1}{q^2 - m_V^2 - \Sigma_V(q^2)} \quad (4)$$

where m_V is the bare mass of the meson and Σ_V the corresponding self-energy of the particle, related to its decay width. Whereas the self-energy in the vacuum can be deduced from experimental measurements of inelastic electron-positron scattering $e^+e^- \rightarrow \text{hadrons}$, the situation for finite T and μ_B is more complicated and requires detailed model calculations. For the present work we apply the results from equilibrium quantum-field theory calculations with a hadronic many-body approach [58, 59]. They account for the interactions of the ρ and ω mesons with hadrons in a heat bath. For the ρ the pion cloud ($\Sigma_{\rho\pi\pi}$) as well as the direct contributions ρ -hadron

scatterings with baryons ($\Sigma_{\rho B}$) and mesons ($\Sigma_{\rho M}$) are included in the calculation of the in-medium self-energy. In this case Eq. 4 becomes

$$D_\rho = \frac{1}{M^2 - m_\rho^2 - \Sigma_{\rho\pi\pi} - \Sigma_{\rho B} - \Sigma_{\rho M}}. \quad (5)$$

The situation for the ω meson is more complex, as it constitutes a three-pion resonance. Here the self energy includes $\omega \rightarrow \pi\rho$ and $\omega \rightarrow 3\pi$ decays as well as the inelastic $\omega\pi \rightarrow \pi\pi$, $\omega\pi \rightarrow b_1$ and $\omega N \rightarrow N^*$ scatterings. The resulting propagator reads

$$D_\omega = [M^2 - m_\omega^2 + i m_\omega (\Gamma_{3\pi} + \Gamma_{\rho\pi} + \Gamma_{\omega\pi \rightarrow \pi\pi}) - \Sigma_{\omega\pi b_1} - \Sigma_{\omega B}]^{-1}. \quad (6)$$

To account for the symmetry of the interactions of ρ and ω mesons with baryons and anti-baryons, the spectral functions do not depend on the baryochemical potential μ_B but on an effective baryon density $\rho_B^{\text{eff}} = \rho_N + \rho_{\bar{N}} + 0.5(\rho_{B^*} + \rho_{\bar{B}^*})$ [60]. Here ρ_N/\bar{N} denotes the nucleon / anti-nucleon density and ρ_{B^*}/\bar{B}^* is the density of excited baryon/anti-baryon resonances.

Note that in the case of a finite pion chemical potential an additional fugacity factor

$$z_\pi^n = \exp\left(\frac{n\mu_\pi}{T}\right) \quad (7)$$

enters in Eq. 3. The exponent n depends on the difference between initial and final pion number for the relevant channel [55, 61, 62]. For dilepton production from ρ mesons one has $n = 2$ whereas for the ω it is $n = 3$.

At the higher masses above $1 \text{ GeV}/c^2$ one no longer finds distinct resonances in the hadronic domain of the vector channel but a broad continuum of multi-pion states which couple to the electromagnetic current. In principle, also here the dilepton emission is related to the vector spectral function. However, the presence of pions at finite T causes a chiral mixing of the isovector part of the vector and axial-vector correlators [63]. The corresponding isovector-vector current correlation function takes the form [64]

$$\Pi_V(p) = (1 - \varepsilon) z_\pi^4 \Pi_{V,4\pi}^{\text{vac}} + \frac{\varepsilon}{2} z_\pi^3 \Pi_{A,3\pi}^{\text{vac}} + \frac{\varepsilon}{2} (z_\pi^4 + z_\pi^5) \Pi_{A,5\pi}^{\text{vac}}, \quad (8)$$

where the mixing coefficient ε is given by the thermal pion loop, and z_π again denotes the pion fugacity.

For temperatures above the critical temperature T_c the relevant degrees of freedom are no longer hadrons (vector mesons) but quarks and gluons. In this situation the strength of the electromagnetic current is accounted for by a partonic description and the thermal dilepton production occurs—to leading order—via the electromagnetic annihilation of quark-antiquark pairs, $q\bar{q} \rightarrow \gamma^*$. However, it has been shown that the pure pQCD result [65] underestimates the actual dilepton emission in the

low energy regime (i.e., at low masses). Nonperturbative results indicate a strong enhancement due to α_s corrections and bremsstrahlung effects [66]. In the present work we apply a spectral function from lattice QCD calculations [67] which has been extrapolated for finite three-momenta by a fit to the according photon rate [11]. Note that these lattice rates are available only for vanishing quark chemical potential $\mu_q = 1/3\mu_B = 0$. However, the effects of a finite μ_q are quite small with regard to the dilepton emission rates and can be neglected here.

D. Non-thermal hadronic decay contributions

In addition to the thermal dilepton emission from the hot and dense fireball, there are also contributions from more long-lived mesons which mostly decay into lepton pairs after the freeze-out of the system, mainly the pseudoscalar π^0 and η mesons. Their Dalitz decays into a real and a virtual photon (which subsequently transforms in a lepton pair) dominate the very low invariant masses. The corresponding decay width is related to the probability for the decay into two photons and given by the Kroll-Wada formula [68]

$$\frac{d\Gamma_{P \rightarrow \gamma e^+ e^-}}{dM} = \frac{2\alpha}{3\pi M} L(M) 2\Gamma_{P \rightarrow \gamma\gamma} \times \left(1 - \frac{M^2}{M_\rho^2}\right) |F_{P\gamma\gamma^*}(M^2)|, \quad (9)$$

where the form factors $F_{P\gamma\gamma^*}$ are fitted to experimental data [69], consistent with the theoretical results assuming VMD.

Note that only the final state π and η mesons are considered for the procedure. Those mesons which are produced and absorbed again during the collision have a negligible probability for a dilepton decay due to their small decay width. The situation is somewhat different for the ϕ meson. In spite of the shorter lifetime we do not treat it as a thermal contribution (since the expected medium-effects are so small that they can be neglected) but consider the microscopic decays here as for the pseudoscalar mesons. However, in this case one assumes that the ϕ has an equal probability for the decay into a lepton pair at any time and therefore can continuously emit dileptons [70]. The total yield is then obtained as a time integral over the lifetime as [17]

$$\frac{dN_{ll}}{dM} = \frac{\Delta N_{ll}}{\Delta M} = \sum_{i=1}^{N_{\Delta M}} \sum_{j=1}^{N_\phi} \int_{t_i}^{t_f} \frac{dt}{\gamma} \frac{\Gamma_{\phi \rightarrow ll}(M)}{\Delta M}, \quad (10)$$

where the γ factor accounts for the relativistic time dilation in the computational frame compared to the meson's rest frame. This procedure explicitly takes absorption processes for the ϕ into account.

Besides, two more non-thermal contributions arise due to the fact that not for all cells it is possible to properly calculate the thermal contribution. This is mainly the

case for the later stages of the reaction, for cells with (i) no baryon content, so that the LRF is not well-defined, or (ii) where the temperature is below 50 MeV, in which case the EoS and the emission rates no longer give reliable results. In these cases a “freeze-out” contribution for the ρ and ω meson is determined directly from the microscopic UrQMD results for those specific cells. The procedure is the same as for the ϕ given by Eq. 10, but the time-integration is performed only for the corresponding time-step size.

III. RESULTS

For the present study the coarse-graining of the UrQMD transport output was performed with ensembles of 1000 UrQMD events for Au+Au collisions at RHIC and 500 events for Pb+Pb reactions at LHC energies. The time-step size was chosen as $\Delta t = 0.4 - 0.6 \text{ fm}/c$, and the spatial dimensions of the cell are defined as $\Delta x = \Delta y = \Delta z = 0.8 - 0.9 \text{ fm}$, depending on the collision energy. The impact parameter distributions corresponding to different centrality classes were chosen using Glauber-Model fits to experimental data [14, 16]. Note that the minimum bias definitions slightly differ between the STAR and PHENIX collaborations; the former uses 0-80% most central collisions whereas the PHENIX trigger takes 0-92% central collisions into account.

A. Fireball evolution

The thermal dilepton emission from a hot and dense fireball created in a heavy-ion collision is determined by the trajectory of the system within the QCD phase diagram. More precisely, since for each space-time cell different values of temperature and baryochemical potential are obtained within the coarse-graining approach, the overall yield is directly related to the distribution of the thermal four-volume V_4 inside the fireball with regard to T and μ_B . Figure 1 (a) shows the total thermal four-volume summed over all cells in dependence on the respective temperature for Au+Au and Pb+Pb reactions at four different collision energies, from the lowest RHIC to top LHC energies. While for the low temperature range around 100 MeV the differences between the energies are not larger than one order of magnitude, the relative increase of the number of higher temperature cells is much stronger. For $\sqrt{s_{NN}} = 19.6 \text{ GeV}$ one hardly finds cells with temperature above 300 MeV, while at LHC energies there are some cells with up to 800 MeV (few rare cells even reach still higher temperatures up to 1000 MeV, which is not shown here).

When considering the μ_B dependence of the four-volume for the temperature range from 120 to 170 MeV in Figure 1 (b), one also finds that the average baryon chemical potential is decreasing when going to higher collision energies. At $\sqrt{s_{NN}} = 19.6 \text{ GeV}$ the most abundant μ_B

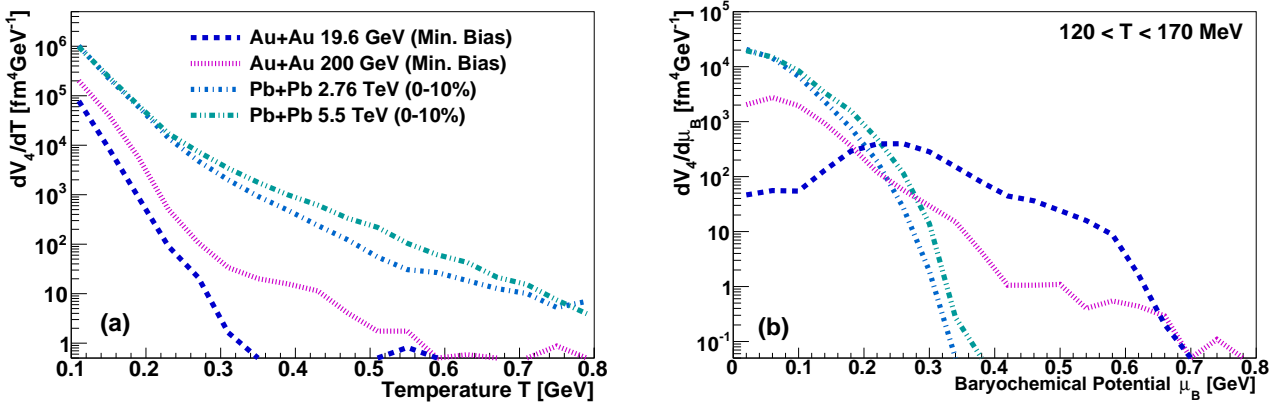


FIG. 1. (Color online) Thermal four-volume V_4 in dependence on temperature (a) and baryochemical potential (b) for Au+Au and Pb+Pb reactions at different collision energies.

range lies between 200 and 300 MeV, whereas at LHC μ_B is close to zero for the overwhelming part of the thermal four-volume. Interesting is the fact that one gets a slightly stronger contribution from higher chemical potential when going from 2.76 to 5.5 GeV. However, this might be an effect due to the limited temperature window considered here.

The resulting time evolution of the thermal dilepton emission dN/dt from all cells (and from those with temperature above 250 MeV only) is shown in Figure 2. The results for central (0-10%) Au+Au reactions at 200 GeV and Pb+Pb collisions at 2.76 TeV exemplarily expose the similarities and differences in the fireball dynamics for RHIC and LHC. In general, one observes that the evolution of the fireball for both energies is very similar, apart

from the larger overall emission at 2.76 TeV compared to the 200 GeV case. This is a consequence of the larger thermal four-volume for all temperature regions, compare Fig. 1 (a). However, at the LHC the cooling of the system is slower, especially the emission from the very hot cells with $T > 250$ MeV shows a less significant drop than for the RHIC energy. In any case, the thermal emission from the later stages of the reaction—even 40-50 fm/c after the first initial nucleon-nucleon interactions—is remarkably large, although the influence on the total yield is very small, as dN/dt is suppressed by 1-2 orders of magnitude compared to the early maxima.

B. Relativistic Heavy-Ion Collider (RHIC)

The dilepton invariant mass spectra for minimum bias Au+Au reactions at the two RHIC energies $\sqrt{s_{NN}} = 19.6$ and 200 GeV are presented in Figure 3. The results as obtained with the coarse-graining approach are compared to the experimental data from the STAR Collaboration [14]. The spectra are shown within the STAR acceptance, which means rapidity and pseudorapidity cuts ($|y^e| < 1$, $|y^{ee}| < 1$) were applied for single electrons and dileptons, respectively, together with an additional transverse momentum cut for electrons (i.e., here $p_t^e > 0.2$ GeV). The comparison shows that in both cases the invariant mass spectra for low masses below 1 GeV/c² are very well described within the model. While in comparison to pure hadronic decay cocktails an excess of the experimentally measured spectra was observed for the mass region $0.3 < M_{e^+e^-} < 0.7$ GeV/c², our approach shows that this region is dominated by thermal emission from the ρ meson and from partonic emission. However, there are also important differences visible when comparing the outcome for both energies: Due to the larger temperatures obtained for Au+Au reactions at 200 GeV, the low mass region is here dominated by QGP emission, only around the ρ pole mass the hadronic emis-

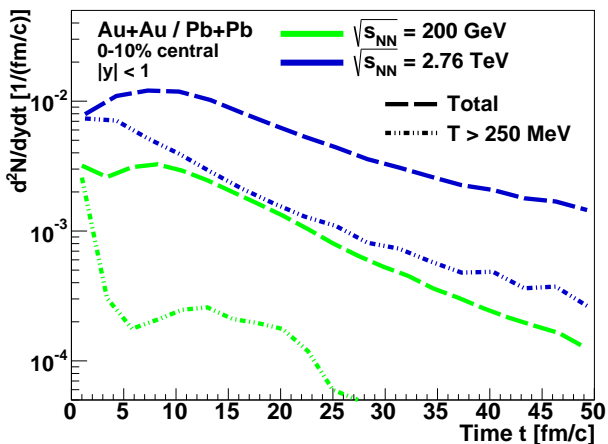


FIG. 2. (Color online) Time evolution of the thermal dilepton emission $dN_{e^+e^-}/dt$ for central Au+Au collisions at $\sqrt{s_{NN}} = 200$ GeV (green) and Pb+Pb collisions at $\sqrt{s_{NN}} = 2.76$ TeV (blue). The total emission (long dashed) is shown as well as the resulting yield only from cells with a temperature above 250 MeV (dashed double-dotted).

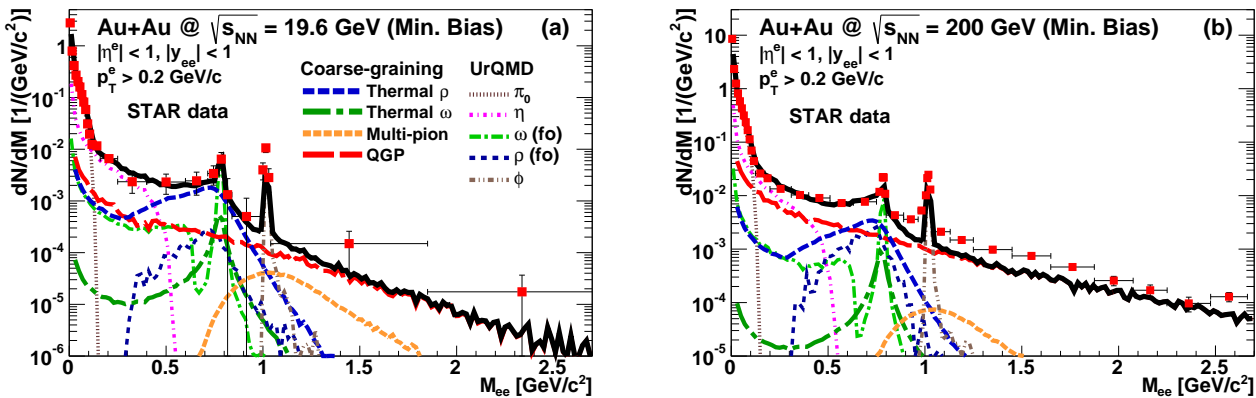


FIG. 3. (Color online) Dielectron invariant spectra for minimum bias (i.e., 0-80% most central) Au+Au collisions at $\sqrt{s_{NN}} = 19.6$ (a) and 200 GeV (b). The sum includes the thermal hadronic and partonic emission obtained with the coarse-graining, and also the hadronic π , η and ϕ decay contributions from UrQMD as well as the “freeze-out” contributions (from cold cells) of the ρ and ω mesons. The model results are compared to the experimental data obtained by the STAR Collaboration [14].

sion is dominant. In contrast, the thermal ρ contribution clearly outshines the partonic yield for the greatest part of the low mass region up to $1\text{ GeV}/c^2$ at the lower collision energy of 19.6 GeV. It is interesting that the spectral shape of the thermal ρ resembles its vacuum shape in both cases, compared to the very strong broadening and low-mass enhancement which is observed for SIS18 and FAIR energies [31, 32]. However, this is not surprising since in the previous section it has already become clear that the baryochemical potential is rather low in most of the cells. And even if one considers that the baryonic modifications of the spectral shape for the

ρ are governed by the effective baryon and anti-baryon density, the effects seem relatively small. One reason for this is that the initial heating is faster and stronger at RHIC energies and the early phase of the reaction is mostly dominated by partonic emission (which is quite insensitive with regard to finite quark chemical potential $\mu_q = 1/3\mu_B$), whereas the hadronic contributions are predominantly radiated at later stages when the baryon densities are lower. Consequently, the baryon-induced medium effects—which are the main cause of the ρ low-mass enhancement—are only very moderate here. Note that there is also a significant non-thermal ρ contribution from low-temperature and late-stage cells, which is more dominant for 200 GeV. This might be due to the longer lifetime of the system, with a significant number of those mesons in peripheral cells and late in the evolution. In contrast to the thermal ρ , the thermal ω contribution is rather negligible compared to the respective freeze-out contribution. This is mainly due to the long lifetime of the ω , which is typically so long that it mostly decays outside the hot and dense region.

In contrast to the low-mass region, for $M_{e^+e^-} > 1\text{ GeV}/c^2$ the overall dilepton yield is no longer dominated by the peaks from various hadronic decays but one experimentally finds a structureless continuum. In our model the thermal emission from multi-pion interactions and from the partonic phase shine in this part of the spectrum. Note however that—as mentioned before—the present calculation does not include the Drell-Yan and, more important, the open-charm contributions to the spectrum. Nevertheless, as the strength of possible medium modification for D or \bar{D} mesons is yet unclear, our calculation can serve as a thermal baseline.

For $\sqrt{s_{NN}} = 19.6\text{ GeV}$ the QGP emission is the dominant contribution in the mass region from 1 to $2.8\text{ GeV}/c^2$ with a significant contribution from the multi-pion part which is strongest around $M_{e^+e^-} = 1.1\text{ GeV}/c^2$. Here 20-

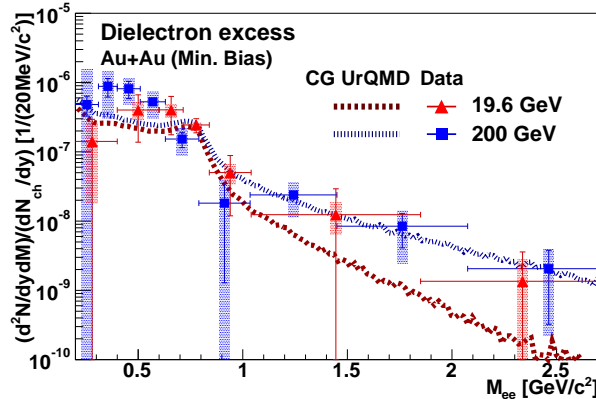


FIG. 4. (Color online) Dielectron excess spectrum for minimum bias (0-80% most central) Au+Au collision at $\sqrt{s} = 19.6$ and 200 AGeV as obtained with the coarse-graining of UrQMD simulations (CG UrQMD). The results include the thermal contributions from the ρ , multi-pion interactions and the QGP. Additionally the UrQMD freeze-out ρ is included for this calculation. The model results are compared to the results of experimental measurements by the STAR Collaboration [15].

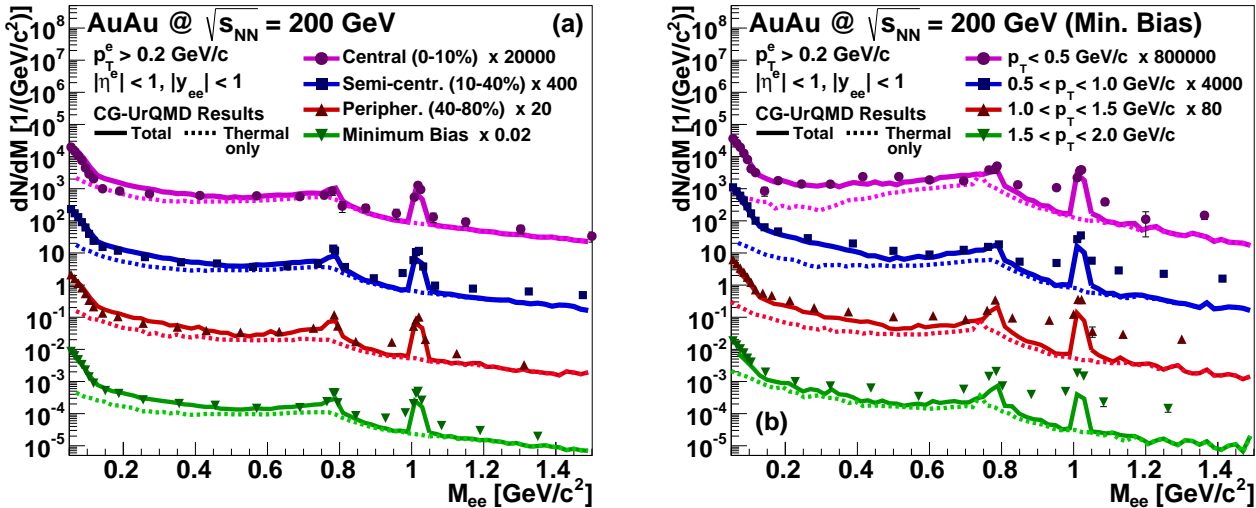


FIG. 5. (Color online) Dielectron invariant mass spectra for Au+Au collisions at $\sqrt{s_{NN}} = 200$ GeV for different centralities (a) and transverse-momentum bins (b). Besides the total yields (full lines) we also show the thermal contribution separately (dashed lines). The results in (a) are shown for central (0-10%), semi-central (10-40%), peripheral (40-80%), and minimum bias (i.e., 0-80%) events. In (b) the spectra are shown for minimum bias collisions in four transverse-momentum bins covering the range from $p_T = 0$ to 2.0 GeV/c. The spectra are shown within the STAR acceptance and compared to the experimental data [14]. In addition, they are scaled for better comparability.

30% of the thermal contribution are from the hadronic source, while for higher masses the multi-pion yield becomes rather insignificant. The comparison with experimental data allows for no clear conclusions at this energy due to the limited statistics and rather large errors. The yield from the coarse-graining model is within the statistical error of the data but rather at the lower bound-

ary. The situation is somewhat different for Au+Au collisions at 200 GeV. At this higher energy the QGP emission is now the dominant thermal contribution, whereas the hadronic contribution is suppressed by at least a factor of 10. Due to the significantly better statistics, one can observe that the model does not fully describe the STAR data, but the dilepton emission obtained within the model makes up for only roughly 50% of the measured yield in the region from 1 to 2 GeV/c 2 . Interestingly, for even higher masses the agreement between model and data becomes better, the slope of the thermal emission seems to be slightly harder than the measured one. These results agree with previous studies indicating that the relative suppression of the charm contribution due to medium effects is more pronounced at higher masses, leaving it the dominant contribution only for lower masses around 1 GeV/c 2 [39].

In addition to the full invariant mass distributions, the STAR Collaboration also published dilepton excess spectra for minimum bias Au+Au collisions at 19.6 and 200 GeV [15]. Here the cocktail contributions (hadronic decays, Drell-Yan and open charm) are subtracted such that the resulting spectra represent only the thermal dilepton emission. Furthermore the data are corrected for the experimental acceptance. In Figure 4 these results are compared to the thermal contribution from our model, including the non-thermal UrQMD “freeze-out” ρ and excluding the thermal ω contribution. (The ω is usually treated as part of the cocktail and was subtracted from the experimental spectrum.) We see that for the mass region $M_{e^+e^-} > 1$ GeV/c 2 in Au+Au col-

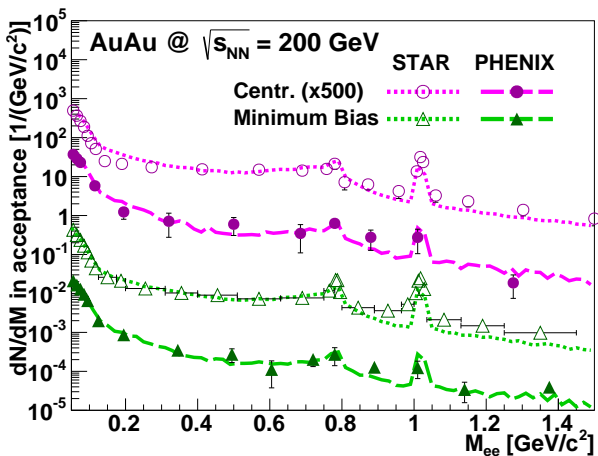


FIG. 6. (Color online) Comparison of the dielectron invariant mass spectra for central (magenta) and minimum bias (green) Au+Au collisions at $\sqrt{s_{NN}} = 200$ GeV with the STAR and PHENIX data [14, 16] in the corresponding acceptances. The total sum of the model results for PHENIX is given by the long dashed lines, and for STAR by the short dashed lines.

lisions at $\sqrt{s_{NN}} = 200$ GeV the thermal result agrees very well with the data, indicating that the thermal part of this mass region seems to be accurately described with the coarse-graining approach. However, note that the subtracted cocktail contribution does not account for medium modifications of the charm contribution, so that the meaning of the high-mass excess spectrum is rather limited. At 19.6 GeV the thermal spectrum from the model seems to be slightly below the data for higher masses, but still within the large statistical and systematic errors. In the low-mass region the agreement between model and data is better for 19.6 GeV than for 200 GeV, but in both cases the experimental thermal excess seems to be slightly underestimated by the model. Nevertheless, considering the uncertainty of the data and the subtraction procedure the agreement is quite satisfactory.

So far we have considered dilepton spectra for minimum bias reactions and the full transverse-momentum range, but the thermal dilepton yield also largely depends on the centrality of the reaction and on the transverse-momentum window in which the results are measured. Both dependencies were investigated by the STAR Collaboration for Au+Au collisions at 200 GeV [14], and the experimental data are presented together with the model results in Figure 5. The left plot (a) shows the invariant-mass spectra for central (0-10%), semi-central (10-40%) and peripheral (40-80%) collisions, together with the minimum bias result from Fig. 3 (b) for comparison. In all four centrality classes one observes quite a good description of the low invariant-mass data by the coarse-graining results. For higher masses larger than $1 \text{ GeV}/c^2$ the underestimation of the dilepton yield observed for minimum bias reactions is also found for other centrality classes. However, for the most central reactions the description seems to be slightly better. In this case the thermal emission alone can almost fully describe the dilepton data for higher masses. This would be in accordance with the assumption that the medium effects on the open charm production are most dominant for central collisions, leading to a suppression of the open-charm contribution to the dilepton spectra.

For the p_t dependence of the e^+e^- production, the comparison between theory and data gives a more nuanced picture, as presented in Figure 5 (b). Here the scaled results for minimum bias Au+Au collisions in four different transverse momentum bins are shown. In the low invariant mass region one finds a good description of the data for the lower transverse momentum bins up to $1 \text{ GeV}/c$, while especially for $p_t > 1.5 \text{ GeV}/c$ the measured results are underestimated by up to a factor 2. Interestingly, this does not only affect the thermal contributions, but also the pure hadronic cocktail contributions, as can be seen from the underestimate for the π dominated very low masses and the ω and ϕ peaks. The reason for this might be the expansion dynamics from the underlying transport model, which is known to somewhat underestimate the collective flow of the fire-

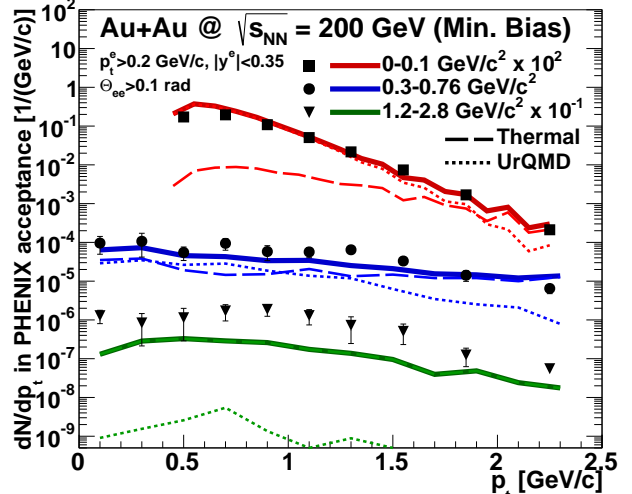


FIG. 7. (Color online) Dielectron transverse-momentum spectra for three mass bins (red: $M = 0 - 0.1 \text{ GeV}/c^2$, blue: $M = 0.3 - 0.76 \text{ GeV}/c^2$, blue: $M = 1.2 - 2.8 \text{ GeV}/c^2$) within the PHENIX acceptance. Besides the total yields from the model calculations (full lines) also the thermal (long dashed) and non-thermal hadronic decay contributions (short dashed) are presented. For comparison the experimental data from the PHENIX Collaboration [16] are shown as well.

ball [71], resulting in too soft p_t spectra for the produced particles. However, the general trend when going from the low to the high transverse momentum region is the increasing importance of the thermal emission in the low-mass region and a flattening of the shape of the spectrum. This is due to two effects: On the one hand, the p_t^e cut for single electrons leads to a suppression of low masses ($M < 0.4 \text{ GeV}/c^2$) when the transverse momentum of the pair is close to zero. On the other hand, the emission of high- p_t dileptons occurs mostly at the higher temperatures which can be found in the early Quark-Gluon Plasma phase, whereas the hadronic emission is usually found to be softer.

Regarding the higher invariant mass region for $M > 1 \text{ GeV}/c^2$, an underestimation of the thermal yield is visible, reaching from a factor 2 for low p_t up to a factor of 10 for the higher transverse momenta. This underprediction is not surprising, as it was already visible in the full p_t -integrated invariant mass spectrum. As mentioned above, this is clearly due to the absence of the charm and Drell-Yan contributions in our calculation.

Although we have up to this point focused on the measurements by the STAR Collaboration, it is natural to compare the model results obtained from the coarse-graining approach also with the results of the PHENIX Collaboration. This is of importance, as the first results from PHENIX showed a strong enhancement of the dilepton invariant mass spectrum for $0.3 < M_{e^+e^-} < 0.7 \text{ GeV}/c^2$ in central collisions, which was not compatible with the results from the STAR Collaboration [72]. In

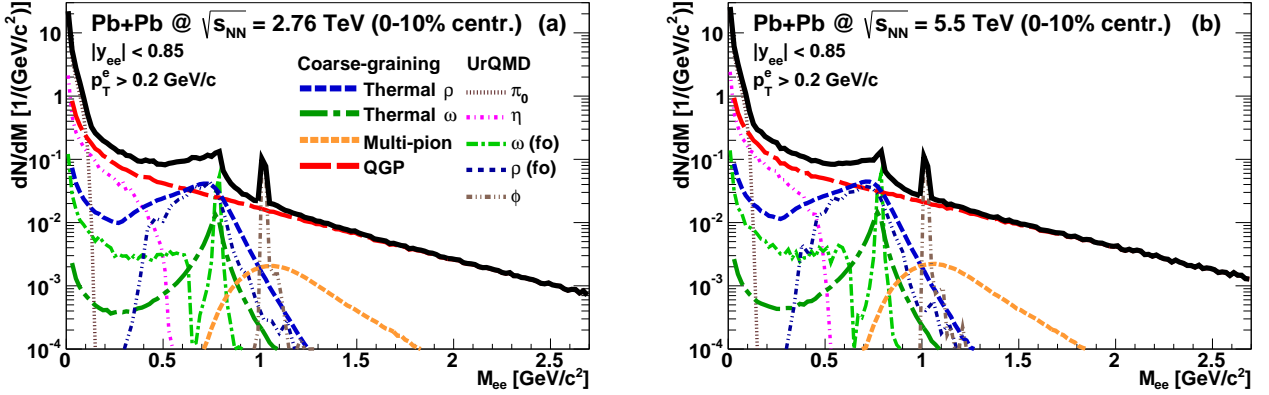


FIG. 8. (Color online) Dielectron invariant spectra for 0-10% most central Pb+Pb collisions at $\sqrt{s_{NN}} = 2.76$ TeV (a) and 5.5 TeV (b). The sum includes the thermal hadronic and partonic emission obtained with the coarse-graining approach, and also the hadronic π , η , and ϕ decay contributions from UrQMD as well as the “freeze-out” contributions (from cold cells) of the ρ and ω mesons.

consequence, there has been a broad discussion about the different detector properties and corresponding acceptances, which made a direct comparison of the two results difficult. Also theoretical models failed to reproduce the PHENIX results [27, 73]. Recently, the PHENIX Collaboration published new results measured with an updated experimental set-up, including a hadron-blind detector (HBD) which could significantly improve the electron

identification and the signal sensitivity [16]. In Figure 6 we show the model results for both central and minimum bias Au+Au collisions at $\sqrt{s_{NN}} = 200$ GeV within the PHENIX and STAR acceptances, together with the corresponding experimental data. The comparison clearly shows that the model not only describes the STAR data, but also the new PHENIX results for central as well as minimum bias collisions. However, note that the statistics obtained by PHENIX is significantly lower, leading to larger errors of the measurement. The main explanation for this is the two-arm set-up of the PHENIX detector so that many of produced electrons and positrons do not reach the detector; if only one particle of a pair reaches the detector, this further increases the background of the measurement. Nevertheless, within the errors of the measurement one can state that the PHENIX and STAR dilepton measurements now fully agree with each other and that the low-mass excess above the hadronic cocktail can be explained by thermal hadronic and partonic emission from medium-modified spectral functions.

To conclude the study for RHIC energies, the model results are finally compared to the transverse momentum spectra from the PHENIX measurement in Figure 7. The (scaled) data and model results within experimental acceptance are presented for three different invariant-mass bins. The thermal contribution and the hadronic decay cocktail from UrQMD are shown separately, as well as the total yield. At very low masses ($M < 0.1$ GeV/ c^2) the hadronic cocktail contribution dominates the dilepton emission, mainly stemming from π^0 decays. Only for high p_t larger than 1.5 GeV/ c the thermal emission becomes significant. However, such high momenta are largely suppressed by a factor of 100 in that mass region. The model results agree quite well with the experimental measurements, only for lower p_t a slight overestimation of the yield is obtained. (Note that dilepton pairs with $p_{t ee} < 0.4$ GeV/ c are out of the PHENIX acceptance in

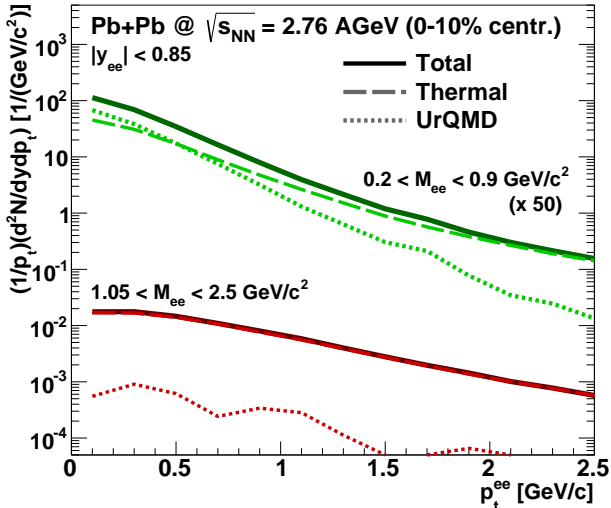


FIG. 9. (Color online) Dielectron transverse-momentum spectra for central Pb+Pb collisions at $\sqrt{s_{NN}} = 2.76$ TeV. The results are shown for the low-mass ($0.2 < M_{e^+e^-} < 0.9$ GeV/ c^2 ; green) and intermediate mass region ($1.05 < M_{e^+e^-} < 2.5$ GeV/ c^2 ; red). Besides the total yields from the model calculations (full lines) also the thermal (long dashed) and non-thermal UrQMD hadronic decay contributions (short dashed) are presented.

this mass bin, as the single electron transverse momentum is required to be larger than $0.2 \text{ GeV}/c$.) In the mass region from 0.3 to $0.76 \text{ GeV}/c^2$ the thermal and nonthermal emission almost equally contribute for low p_t with a slight dominance of the hadronic cocktail for transverse momenta from 0.5 to $1.0 \text{ GeV}/c$. In contrast, the thermal dilepton emission clearly outshines the hadronic decays for higher p_t values above $1.5 \text{ GeV}/c$. Note that the present findings from the coarse-graining approach for this mass region roughly agree with the results from a fireball parametrization (using the same spectral functions as in our model) where the non-thermal emission dominates for lower momenta and the thermal contribution—mainly from the ρ —for higher momenta [16]. For the mass region $M_{e^+e^-} > 1.2 \text{ GeV}/c^2$ the thermal emission (i.e., here almost exclusively the partonic contribution from the QGP) is clearly the dominant source in the present calculations. However, the yield obtained with the coarse-graining approach is below the data about a factor 2-3 for low p_t and up to 10 for higher momenta, once again indicating the missing contributions from open-charm mesons. In spite of the significantly differing acceptances of the STAR and PHENIX experiments, the present results are consistent with the findings from the comparison of the model outcome and STAR data for the invariant mass spectra in various p_t -bins (see Fig. 5 (b)).

C. Large Hadron Collider (LHC)

As became clear from the study of the reaction dynamics in Sec. III A, the fireball of hot and dense matter created in a heavy-ion collision reaches higher temperatures and cools down more slowly at the Large Hadron Collider in comparison to the reaction evolution for RHIC energies. However, there is no significant change with regard to the baryon densities, the baryochemical potential was already close to zero for most cells $\sqrt{s_{NN}} = 200 \text{ GeV}$. Consequently, the resulting invariant mass spectra for central (0-10%) Pb+Pb collisions at center-of-mass energies of 2.76 and 5.5 TeV as shown in Figure 8 exhibit the same mostly vacuum-like spectral shape of the ρ meson contribution, together with an increased yield stemming from the Quark-Gluon Plasma. The partonic contribution is dominating the spectra for masses above $0.1 \text{ GeV}/c^2$, except for the pole-mass peaks of the three vector mesons ρ , ω and ϕ . However, the ρ contribution still plays a significant role as well, and its relative strength is not much smaller than at the top RHIC energy. In general, the increasing number of hot cells with temperature above T_c goes along with a longer lifetime of the fireball and a larger overall thermal four-volume also for temperatures below the critical temperature, which equally leads to a rise of the hadronic emission. In the same manner as there is no strong change of the spectra from RHIC to LHC, the situation does hardly change when going from 2.76 TeV to the maximum LHC energy

of 5.5 TeV , except for an higher overall yield. We will study this energy dependence in more detail in Sec. III D.

The transverse momentum spectra for 2.76 TeV in Figure 9 are shown in two different mass bins, for the low-mass region ($0.2 < M_{e^+e^-} < 0.9 \text{ GeV}/c^2$) and for the masses above the ϕ pole mass ($1.05 < M_{e^+e^-} < 2.5 \text{ GeV}/c^2$). For the lower masses the finding is similar to those for Au+Au collisions at 200 GeV (compare Fig. 7): The hadronic sources are more dominant at low p_t , while the thermal emission is the major contribution for high momenta. In general the slope of the thermal emission is harder (i.e., flatter) than that of the hadronic decays. For the mass region above $1 \text{ GeV}/c^2$, the only dominant contribution stems from the Quark-Gluon Plasma, whereas the hadronic decays become negligible. The overall slope of the higher masses is also harder, indicating emission from hotter cells on the one hand, but also the stronger flow which is proportional to the mass of the particles. As before one should, however, bear in mind that a full study for the high masses would need to include the missing charm (and Drell-Yan) contributions.

D. Comparison of RHIC and LHC results

The previous results have already shown that the temperature and lifetime of the fireball increase when going from RHIC to LHC energies, which is connected with a larger yield from thermal dilepton production. In the following, these very qualitative findings shall be investigated in more detail.

In Figure 10 (a) the relative ratio of the thermal dilepton yield at mid-rapidity ($|y_{ee}| < 1$) for different mass regions is shown in relation to the yield which is obtained for Au+Au collisions at $\sqrt{s_{NN}} = 200 \text{ GeV}$. In addition, the increase of the π^0 yield is shown, as comparison of the thermal results with the production of hadrons or dileptons from hadronic decays, respectively. The results depict that in general the thermal contributions exhibit a stronger increase than the π^0 yield. For the lower masses—0.05 to 0.3 and 0.3 to $0.6 \text{ GeV}/c^2$ —the thermal yield scales with the number of neutral pions as $N_{\pi^0}^\alpha$, with α found to be approximately 1.9 here. For the mass region above the ϕ pole mass, where purely the QGP contributes to the thermal emission, the relative increase is even stronger with $\alpha \approx 2.4$. Note that the exponent α for the mass region where the excess above the cocktail is found (i.e., 0.3 - $0.6 \text{ GeV}/c^2$) is similar and only slightly larger compared to the one obtained using a fireball parametrization [11]; there the scaling with the total number of charged hadronic particles is found to be N_{ch}^α and $\alpha = 1.8$. The somewhat stronger enhancement of the high-mass yield at LHC energies is not surprising, as the number of QGP emitting hot cells exhibits a larger increase than the lower temperature four-volume (compare Figs. 1 and 2).

Whereas the thermal yields alone allow for only rather

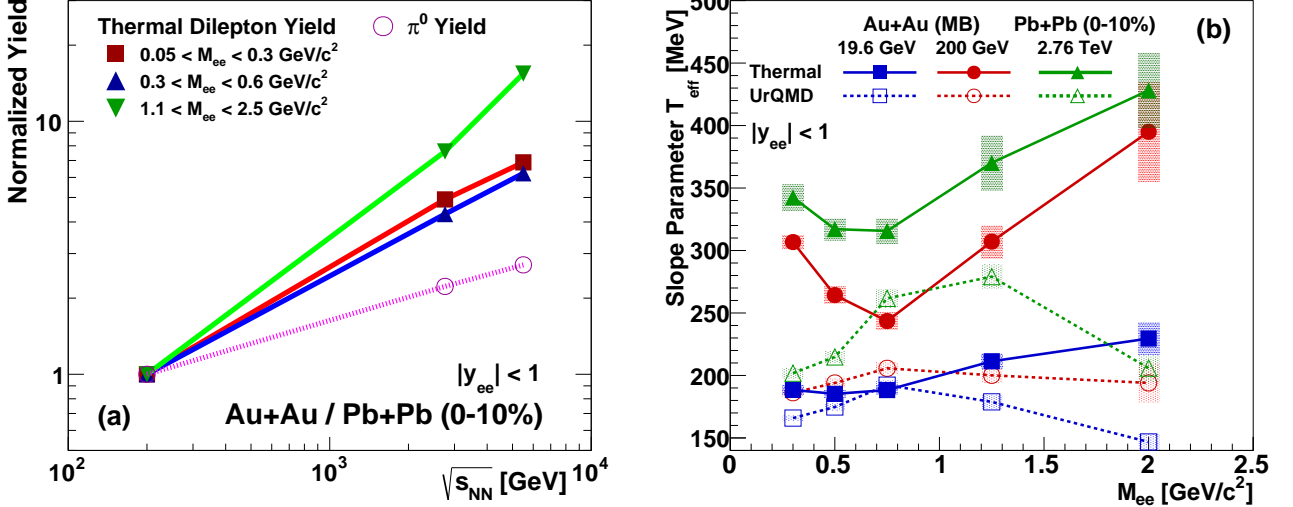


FIG. 10. (Color online) (a) Thermal dilepton yield for three different mass regions and the π^0 yield for central Au+Au/Pb+Pb collisions, normalized to the result for $\sqrt{s_{NN}} = 200 \text{ GeV}$. (b) Mass dependent slope parameter T_{eff} for the thermal (full lines) and non-thermal (dashed lines) dilepton yields in minimum bias Au+Au collisions at 19.6 GeV (blue) and 200 GeV as well as for central Pb+Pb at 2.76 TeV (green). The error bands indicate the systematic error of the fit. All results are for mid-rapidity, i.e., for $|y_{ee}| < 1$.

qualitative conclusions regarding the underlying reaction dynamics, another observable that helps to determine the temperature and expansion dynamics of the created fireball is the slope of the transverse-mass spectra ($m_t = \sqrt{M_{ee}^2 + p_t^2}$). The effective slope parameter T_{eff} can be extracted using the fit function [74]

$$\frac{dN}{m_t dm_t} = C \cdot \exp\left(-\frac{m_t}{T_{\text{eff}}}\right). \quad (11)$$

Note that T_{eff} must not be confounded with the temperature of the medium, as the transverse momentum distribution from a thermal source is not only determined by the temperature: The radial flow of the system leads to a significant blue-shift of the m_t spectra as well [11]. The effective slope parameter for the thermal and hadronic cocktail (UrQMD) contributions at mid-rapidity for Au+Au and Pb+Pb collisions at three different energies ($\sqrt{s_{NN}} = 19.6, 200) is shown in Figure 10(b). The results are presented for different mass bins ranging from 0.2 to $2.5 \text{ GeV}/c^2$. To obtain T_{eff} the spectra were fitted in mass-dependent m_t -ranges corresponding to $0.5 < p_t < 1.8 \text{ GeV}/c$. Interestingly, the results exhibit completely different mass-dependencies for thermal and non-thermal contributions. T_{eff} of the non-thermal decay contributions reaches a maximum around the ρ and ω pole masses (for RHIC energies) or around $1-1.5 \text{ GeV}/c^2$ (at LHC) and falls off when going to lower or higher energies. Conversely, the slope parameter of the thermal contributions drops with increasing mass or remains at the same level up to approximately $1 \text{ GeV}/c^2$ and then it shows a strong rise for higher masses.$

The different mass-dependency of T_{eff} for the thermal and non-thermal decay contributions can be explained by the different conditions of emission: Where the thermal source is mainly of hadronic nature, i.e., especially around the ρ and ω pole masses, one finds a lower average emission temperature, compared to the mass ranges dominated by the partonic contribution. This effect is reflected in the thermal m_t -slopes. The increase of T_{eff} for masses above $1 \text{ GeV}/c^2$ is due to the fact that the thermal high mass emission is suppressed at lower temperatures. In contrast, the non-thermal hadronic decays mostly occur at a late stage of the fireball evolution, outside the hot and dense region. This leads to in general lower slope parameters obtained for the non-thermal contributions compared to the thermal ones. However, note that there is a difference between the contributions from the long-lived low-mass π^0 and η mesons, for which one finds the lowest T_{eff} , and especially the very short-lived freeze-out ρ contribution. In spite of the fact that here the ρ stems only from cells where no thermal emission is assumed, in its pole mass region one finds a harder slope than at the π^0 and η dominated low-masses. A reason might also be that these ρ mesons carry additional momentum due to their rather late and peripheral origin, compared to the other mesons. The decrease for higher masses above $1 \text{ GeV}/c^2$ —which are dominated by the ϕ and still some ρ —might be explained by the kinematics of the microscopic decay processes, where high momenta are naturally suppressed if a particle with higher mass is produced, and the longer lifetime of the ϕ compared to the ρ meson.

The slope parameters for the thermal emission from

the coarse-graining approach are similar to those from a fireball parametrization [11] for RHIC energies, but for the LHC they seem to be somewhat smaller. However, as already mentioned, it is known that the flow effects are underestimated within the UrQMD model at high collision energies [71], so that these differences should be mainly due to a less distinct expansion of the system and not due to differences in the average temperature. The same conclusion is suggested by the comparison of dilepton spectra with experimental data, where we saw an underestimation of the yield for high- p_t (see, e.g., Fig. 5 (b)).

IV. CONCLUSIONS & OUTLOOK

In this paper we have presented dilepton spectra for energies available at collider energies, obtained with an approach using coarse-grained UrQMD transport simulations to calculate the thermal dilepton emission. The results for RHIC energies are compared with the experimental data from the STAR and PHENIX Collaborations and show good agreement. Furthermore, we could depict that the newest PHENIX results collected with the HBD upgrade of the detector are now fully consistent with the STAR measurements and can both be reproduced within the coarse-graining approach. The excess above the hadronic cocktail in the region for $0.3 < M_{e^+e^-} < 0.7 \text{ GeV}/c^2$ is hereby explained by thermal emission from a broadened ρ and the Quark-Gluon Plasma.

For higher masses above the ϕ peak our results lie by tendency somewhat below the experimental data. This can be mainly ascribed to the missing implementation of the charm emission, which will be the dominant source for these high masses. However, our results show that also the partonic emission gives a significant contribution to the overall yield in this mass region. The present results are consistent with the open charm dilepton spectra obtained using a Langevin approach to simulate the in-medium effects on the invariant mass spectra. These simulations indicate a strong suppression of the open charm contribution inside hot and dense matter compared to the vacuum case and making up only roughly 50% of the total yield [39]. In consequence, a study of dilepton emission including the charm contribution in the coarse-

graining approach would be very instructive for the full understanding of the dilepton emission for higher masses and is planned for future investigations.

While the energy and centrality dependence of the dilepton production are well reproduced within the model, the transverse-momentum dependence shows some deviations from the measurement for higher p_t , whereas the (dominant) low-momentum production is quite well described. This effect is probably connected to an underestimation of the collective flow in the underlying transport model. One should bear in mind that the model is purely hadronic and that it might therefore not be able to describe some dynamical effects adequately, which are due to the emergence of a partonic phase. However, considering the hadronic nature of the model, the agreement with experimental data as well as the spectra from fireball parametrizations is surprisingly good. In consequence, this substantiates the basic idea of the coarse-graining approach, namely that the only necessary information regarding the fireball evolution is energy and particle density (or T and μ , respectively), if one wants to determine the dilepton emission.

Together with the previous results for SIS 18, FAIR and CERN-SPS energies, the coarse-graining approach has proven a successful tool for the theoretical description of dilepton production in heavy-ion collisions over the whole range of presently available energies, corresponding to a range of $\sqrt{s_{NN}}$ which spans over three orders of magnitude.

ACKNOWLEDGMENTS

The authors especially thank Ralf Rapp for providing the parametrizations of the spectral functions. S. E. acknowledges Jan Steinheimer for valuable and fruitful discussions. This work was supported by the Hessian Initiative for Excellence (LOEWE) through the Helmholtz International Center for FAIR (HIC for FAIR), the Bundesministerium für Bildung und Forschung, Germany (BMBF) and the Helmholtz-Gemeinschaft through the Research School for Quark-Matter Studies (H-QM). The computational resources for this work were provided by the LOEWE-CSC.

[1] H. Stöcker and W. Greiner, *Phys. Rept.* **137**, 277 (1986).
[2] P. Danielewicz, R. Lacey, and W. G. Lynch, *Science* **298**, 1592 (2002).
[3] E. Shuryak, *Prog. Part. Nucl. Phys.* **62**, 48 (2009).
[4] R. Rapp, J. Wambach, and H. van Hees, in R. Stock (ed.), *Relativistic Heavy Ion Physics*, vol. 23 of *Landolt-Börnstein - Group I Elementary Particles, Nuclei and Atoms*, 134–175 (Springer, Berlin, 2010).
[5] J. Schukraft and R. Stock, in H. Schopper and L. Di Lella (eds.), *60 Years of CERN Experiments and Discoveries*, chap. 3, 61–87 (World Scientific, Singapore, 2015).
[6] J. D. Bjorken, *Phys. Rev. D* **27**, 140 (1983).
[7] E. L. Feinberg, *Nuovo Cim. A* **34**, 391 (1976).
[8] E. V. Shuryak, *Phys. Lett. B* **78**, 150 (1978).
[9] G. Vujanovic, C. Young, B. Schenke, R. Rapp, S. Jeon, et al., *Phys. Rev. C* **89**, 034904 (2014).
[10] R. Ryblewski and M. Strickland, *Phys. Rev. D* **92**, 025026 (2015).
[11] R. Rapp, *Adv. High Energy Phys.* **2013**, 148253 (2013).
[12] R. Rapp and H. van Hees, *Phys. Lett. B* **753**, 586 (2016).

[13] L. Adamczyk et al. (STAR Collaboration), Phys. Rev. Lett. **113**, 022301 (2014), [Addendum: Phys. Rev. Lett. **113**, 049903 (2014)].

[14] L. Adamczyk et al. (STAR Collaboration), Phys. Rev. C **92**, 024912 (2015).

[15] L. Adamczyk et al. (STAR Collaboration), Phys. Lett. B **750**, 64 (2015).

[16] A. Adare et al. (PHENIX Collaboration), Phys. Rev. C **93**, 014904 (2016).

[17] K. Schmidt, E. Santini, S. Vogel, C. Sturm, M. Bleicher, et al., Phys. Rev. C **79**, 064908 (2009).

[18] J. Weil, H. van Hees, and U. Mosel, Eur. Phys. J. A **48**, 111 (2012).

[19] J. Weil, S. Endres, H. van Hees, M. Bleicher, and U. Mosel, J. Phys. Conf. Ser. **612**, 012039 (2015).

[20] S. Endres and M. Bleicher, J. Phys. Conf. Ser. **426**, 012033 (2013).

[21] E. Bratkovskaya, J. Aichelin, M. Thomere, S. Vogel, and M. Bleicher, Phys. Rev. C **87**, 064907 (2013).

[22] B. Schenke and C. Greiner, Phys. Rev. C **73**, 034909 (2006).

[23] B. Schenke and C. Greiner, Phys. Rev. Lett. **98**, 022301 (2007).

[24] J. Weil, U. Mosel, and V. Metag, Phys. Lett. B **723**, 120 (2013).

[25] E. L. Bratkovskaya, W. Cassing, R. Rapp, and J. Wambach, Nucl. Phys. A **634**, 168 (1998).

[26] E. Bratkovskaya and W. Cassing, Nucl. Phys. A **807**, 214 (2008).

[27] O. Linnyk, W. Cassing, J. Manninen, E. L. Bratkovskaya, and C. M. Ko, Phys. Rev. C **85**, 024910 (2012).

[28] O. Linnyk, E. L. Bratkovskaya, and W. Cassing, Prog. Part. Nucl. Phys. **87**, 50 (2016), 1512.08126.

[29] P. Huovinen, M. Belkacem, P. J. Ellis, and J. I. Kapusta, Phys. Rev. C **66**, 014903 (2002).

[30] S. Endres, H. van Hees, J. Weil, and M. Bleicher, Phys. Rev. C **91**, 054911 (2015).

[31] S. Endres, H. van Hees, J. Weil, and M. Bleicher, Phys. Rev. C **92**, 014911 (2015).

[32] S. Endres, H. van Hees, and M. Bleicher (2015), arXiv: 1512.06549 [nucl-th].

[33] J. Steinheimer, M. Lorenz, F. Becattini, R. Stock, and M. Bleicher (2016), arXiv: 1603.02051 [nucl-th].

[34] S. A. Bass, M. Belkacem, M. Bleicher, M. Brandstetter, L. Bravina, et al., Prog. Part. Nucl. Phys. **41**, 255 (1998).

[35] M. Bleicher, E. Zabrodin, C. Spieles, S. A. Bass, C. Ernst, et al., J. Phys. G **25**, 1859 (1999).

[36] A. Adare et al. (PHENIX Collaboration), Phys. Lett. B **670**, 313 (2009).

[37] H. van Hees and R. Rapp, Phys. Rev. C **71**, 034907 (2005).

[38] T. Lang, H. van Hees, J. Steinheimer, G. Inghirami, and M. Bleicher, Phys. Rev. C **93**, 014901 (2016).

[39] T. Lang, H. van Hees, J. Steinheimer, and M. Bleicher (2013), arXiv: 1305.7377 [hep-ph].

[40] G. David, R. Rapp, and Z. Xu, Phys. Rept. **462**, 176 (2008).

[41] A. Adare et al. (PHENIX Collaboration), Phys. Rev. Lett. **109**, 122302 (2012).

[42] A. Adare et al. (PHENIX Collaboration) (2015), arXiv: 1509.07758 [nucl-ex].

[43] H. Petersen, M. Bleicher, S. A. Bass, and H. Stöcker (2008), arXiv: 0805.0567 [hep-ph].

[44] <http://www.urqmd.org>.

[45] W. M. Yao et al. (Particle Data Group), J. Phys. G **33**, 1 (2006).

[46] C. Eckart, Phys. Rev. **58**, 919 (1940).

[47] D. Zschiesche, S. Schramm, J. Schaffner-Bielich, H. Stöcker, and W. Greiner, Phys. Lett. B **547**, 7 (2002).

[48] M. He, R. J. Fries, and R. Rapp, Phys. Rev. C **85**, 044911 (2012).

[49] L. Bravina, E. Zabrodin, M. I. Gorenstein, S. Bass, M. Belkacem, et al., Nucl. Phys. A **661**, 600 (1999).

[50] L. Bravina, E. Zabrodin, M. I. Gorenstein, S. Bass, M. Belkacem, et al., Phys. Rev. C **60**, 024904 (1999).

[51] W. Florkowski and R. Ryblewski, Phys. Rev. C **83**, 034907 (2011).

[52] W. Florkowski, M. Martinez, R. Ryblewski, and M. Strickland, Nucl. Phys. A **904-905**, 803c (2013).

[53] D. Bandyopadhyay, M. Gorenstein, H. Stöcker, W. Greiner, and H. Sorge, Z. Phys. C **58**, 461 (1993).

[54] P. Koch, Phys. Lett. B **288**, 187 (1992).

[55] R. Rapp and J. Wambach, Adv. Nucl. Phys. **25**, 1 (2000).

[56] F. Klingl, N. Kaiser, and W. Weise, Nucl. Phys. A **624**, 527 (1997).

[57] L. D. McLerran and T. Toimela, Phys. Rev. D **31**, 545 (1985).

[58] R. Rapp and J. Wambach, Eur. Phys. J. A **6**, 415 (1999).

[59] R. Rapp (2014), private communication.

[60] H. van Hees and R. Rapp, Nucl. Phys. A **806**, 339 (2008).

[61] R. Baier, M. Dirks, and K. Redlich, Acta Phys. Polon. B **28**, 2873 (1997).

[62] R. Baier, M. Dirks, K. Redlich, and D. Schiff, Phys. Rev. D **56**, 2548 (1997).

[63] M. Dey, V. Eletsky, and B. L. Ioffe, Phys. Lett. B **252**, 620 (1990).

[64] H. van Hees and R. Rapp, Phys. Rev. Lett. **97**, 102301 (2006).

[65] J. Cleymans, J. Fingberg, and K. Redlich, Phys. Rev. D **35**, 2153 (1987).

[66] E. Braaten, R. D. Pisarski, and T.-C. Yuan, Phys. Rev. Lett. **64**, 2242 (1990).

[67] H.-T. Ding, A. Francis, O. Kaczmarek, F. Karsch, E. Laermann, et al., Phys. Rev. D **83**, 034504 (2011).

[68] N. M. Kroll and W. Wada, Phys. Rev. **98**, 1355 (1955).

[69] L. G. Landsberg, Phys. Rept. **128**, 301 (1985).

[70] G.-Q. Li and C. M. Ko, Nucl. Phys. A **582**, 731 (1995).

[71] H. Petersen, Q. Li, X. Zhu, and M. Bleicher, Phys. Rev. C **74**, 064908 (2006).

[72] A. Adare et al. (PHENIX Collaboration), Phys. Rev. C **81**, 034911 (2010).

[73] R. Rapp, AIP Conf. Proc. **1322**, 55 (2010).

[74] T. Renk and J. Ruppert, Phys. Rev. C **77**, 024907 (2008).